

1 **Testing the assumptions underlying ocean mixing methodologies using**
2 **direct numerical simulations**

3 J.R. Taylor*

4 *Department of Applied Mathematics and Theoretical Physics, University of Cambridge,*
5 *Cambridge, CB3 0WA, U.K.*

6 S.M. de Bruyn Kops

7 *Department of Mechanical and Industrial Engineering, University of Massachusetts Amherst,*
8 *Amherst, Massachusetts, USA 01003*

9 C. P. Caulfield

10 *BP Institute & Department of Applied Mathematics and Theoretical Physics*
11 *University of Cambridge, Cambridge, CB3 0EZ, U.K.*

12 P.F. Linden

13 *Department of Applied Mathematics and Theoretical Physics, University of Cambridge,*
14 *Cambridge, CB3 0WA, U.K.*

15 * *Corresponding author address:* John R. Taylor, CMS, DAMTP, University of Cambridge, Wilber-
16 force Road, Cambridge, UK, CB3 0WA.

17 E-mail: J.R.Taylor@damtp.cam.ac.uk

ABSTRACT

18 Direct numerical simulations of stratified turbulence are used to test several
19 fundamental assumptions involved in the Osborn, Osborn-Cox, and Thorpe
20 methods commonly used to estimate the turbulent diffusivity from field mea-
21 surements. The forced simulations in an idealized triply periodic computa-
22 tional domain exhibit characteristic features of stratified turbulence including
23 intermittency and layer formation. When applied using the volume-averaged
24 dissipation rates from the simulations, the vertical diffusivities inferred from
25 the Osborn and Osborn-Cox methods are within 40% of the value diagnosed
26 using the volume-averaged buoyancy flux for all cases, while the Thorpe scale
27 method performs similarly well in the simulation with a relatively large buoy-
28 ancy Reynolds number ($Re_B \simeq 240$) but significantly overestimates the ver-
29 tical diffusivity in simulations with $Re_B < 60$. The methods are also tested
30 using a limited number of vertical profiles randomly selected from the com-
31 putational volume. The Osborn, Osborn-Cox and Thorpe scale methods con-
32 verge to their respective estimates based on volume-averaged statistics faster
33 than the vertical diffusivity calculated directly from the buoyancy flux which
34 is contaminated with reversible contributions from internal waves. In terms
35 of the relative error the Osborn method outperforms two of the underlying
36 assumptions associated with the method. Motivated by a recent theoretical
37 development, it is speculated that the Osborn method might provide a reason-
38 able approximation to the diffusivity associated with the *irreversible* buoy-
39 ancy flux.

40 1. Introduction

41 Small-scale turbulence, defined here as three-dimensional overturning motions, plays an impor-
42 tant role in setting the large-scale properties and circulation of the ocean. Turbulence influences
43 the depth of the surface and bottom mixed layers by entraining stratified water into the mixed
44 layer (e.g. Large et al. (1994); Pacanowski and Philander (1981)) thereby influencing biological
45 productivity and the exchanges of heat and carbon between the atmosphere and ocean (Marra et al.
46 1990). On long timescales, turbulence gradually mixes distinct water masses in the ocean interior,
47 thereby influencing the pathways of the global overturning circulation (Wunsch and Ferrari 2004;
48 Marshall and Speer 2012).

49 Here we use the term ‘mixing’ to refer to the irreversible homogenization of a scalar quantity.
50 This stands in contrast to ‘stirring’ which refers to the down-scale transfer of scalar variance and
51 the generation of structures such as filaments by turbulent motions. Mixing relies on molecular
52 diffusion of the scalar substance (e.g. heat or salt) which occurs at very small scales, while stirring
53 is inevitably associated with larger scales. For a statistically homogeneous turbulent flow, mixing
54 occurs at scales close to the Batchelor scale, $l_B = l_K / \sqrt{Pr}$ where $l_K = (\nu^3 / \epsilon)^{1/4}$ is the Kolmogorov
55 scale, $Pr = \nu / \kappa_m$ is the Prandtl (or Schmidt) number, ν is the kinematic viscosity, κ_m is the
56 molecular scalar diffusivity, and ϵ is the dissipation rate of kinetic energy. For typical open ocean
57 conditions where $\epsilon = 10^{-10} - 10^{-6} \text{m}^2/\text{s}^3$, the corresponding Kolmogorov scale is $l_K = 1 \text{mm} -$
58 1cm and the thermal Batchelor scale is $l_B \simeq 0.3 - 3 \text{mm}$ while the haline Batchelor scale is an order
59 of magnitude smaller. The very small scales involved make it difficult, if not impossible, currently
60 to resolve scalar mixing in measurements or models.

61 Due to the difficulty associated with resolving the small scales involved in scalar mixing, ob-
62 servational methods generally involve calculating various proxies for mixing. A near-universal

63 assumption in the ocean mixing literature is that an ensemble of turbulent motions can be mod-
64 elled through a turbulent diffusivity, defined as the ensemble-averaged scalar flux (in a particular
65 coordinate direction) divided by the ensemble-averaged gradient (in an independently chosen di-
66 rection). Although the turbulent diffusivity is a second rank tensor, our focus here will be on the
67 vertical component, which we define

$$\kappa \equiv \frac{-\langle w'c' \rangle}{\partial \langle c \rangle / \partial z}, \quad (1)$$

68 where c is a scalar quantity, angle brackets indicate an unspecified averaging operator assumed to
69 be equivalent to ensemble-averaging, and primes denote departures from this average. Note that
70 in some contexts (e.g. at fronts or in isopycnal coordinate ocean models) the diapycnal diffusivity
71 might be more appropriate than the vertical diffusivity. In the simulations that will be analyzed
72 here, the large-scale buoyancy gradient is aligned with the vertical direction, and hence the vertical
73 and diapycnal diffusivities are equivalent by construction.

74 Indeed, estimating κ is one of the central aims of the ocean mixing community. Perhaps the
75 most direct approach is to measure the vertical turbulent scalar flux $\langle w'c' \rangle$ through simultaneous
76 measurements of the vertical velocity and scalar concentration. While this method is in princi-
77 ple possible (e.g. Moum (1996)), it can be extremely difficult to measure the vertical velocity
78 accurately, and the correlation between the velocity and scalar concentration introduces another
79 possible source of error. In addition, as we will see later, internal waves can induce a significant
80 *reversible* contribution to the turbulent scalar flux and removing these contributions can be very
81 difficult, not least because the collection of a sufficiently large ensemble of measurements would
82 be prohibitively expensive to collect.

83 Other indirect methods of measuring the turbulent diffusivity necessarily rely on assumptions
84 about the nature of small-scale turbulence. Indirect methods can be arranged in two categories:

85 ‘finescale’ methods and ‘microstructure’ methods, each based around different assumptions. Sev-
86 eral finescale methods rely on the assumption that small-scale turbulence in the ocean interior is
87 forced by the ambient internal wave field. These methods then link the mixing via small-scale
88 turbulence with the properties of the internal wave field (e.g. Henyey et al. (1986); Gregg (1989a);
89 Polzin et al. (1995); MacKinnon and Gregg (2003)).

90 Rather than relying on measurements of internal waves, microstructure methods use measure-
91 ments of small-scale turbulence to infer the turbulent diffusivity. Two prominent microstructure
92 methods are the Osborn-Cox method (Osborn and Cox 1972), which uses measurements of tem-
93 perature or salinity variance and infers the scalar variance dissipation rate and diffusivity; and
94 the Osborn method (Osborn 1980), which relates measurements of shear to the turbulent dissipa-
95 tion rate, and hence to the diffusivity. Gregg et al. (2018) provides a review and discussion of
96 microstructure methods and their underlying assumptions.

97 An additional method for inferring the rate of mixing is the Thorpe-scale method. This method
98 is perhaps best classified as intermediate between finescale and microstruture methods as it uses
99 measurements of the scalar fields to infer the size of the largest turbulent motions. In this method
100 unstable ‘overturns’ in a measured temperature, salinity, or density profile are first related to the
101 dissipation rate and then to the turbulent diffusivity following the Osborn method (Osborn 1980).
102 These methods and their underlying assumptions will be described in more detail in Section c
103 below.

104 The primary objective of this paper is to evaluate microstructure and Thorpe-scale methods using
105 the output from direct numerical simulations (DNS) of forced stratified turbulence. By definition
106 a DNS resolves *all* scales of turbulent motion. The simulations here have a molecular Prandtl
107 number $Pr = 7$, a typical value corresponding to the diffusion of heat in seawater. Hence, the
108 resolution of the simulations must be sufficient to capture scales near the Batchelor scale ($\sim 1\text{mm}$

109 in dimensional terms). Our aim is to simulate typical turbulent conditions in the ocean interior.
110 Even with a limited domain size, this makes the simulations extremely computationally expensive
111 - here the simulations exceed 10^{12} gridpoints. The advantage of DNS is that turbulent quantities
112 such as the dissipation rate and scalar flux can be evaluated exactly. This allows us to distinguish
113 between uncertainties associated with measurement techniques from uncertainties associated with
114 the underlying assumptions inherent in each method. Here, our focus is on such assumption-
115 associated uncertainties.

116 The DNS that are analyzed here simulate turbulence in a relatively small ($\sim 5 - 10\text{m}$) three-
117 dimensional domain. Periodic boundary conditions are applied to the velocity, while a constant
118 vertical background stratification is imposed. The computational domain can be interpreted as
119 a small region embedded in the ocean interior. The simulations are forced by applying a scale-
120 selective deterministic body force to the momentum equations to energize the large scales of the
121 horizontal velocity. While the forcing term is intended to represent energy input from uncaptured
122 large-scale motions, we do not attempt to simulate a particular internal wave spectrum at the large
123 scales. We therefore do not attempt to test any finescale parameterizations and instead focus on
124 microstructure and Thorpe-scale-based methods.

125 Many microstructure measurement techniques involve fitting a canonical spectrum to the mea-
126 sured spectrum obtained from a depth window (Gregg 1999) or spatially averaging over a pre-
127 scribed depth interval (Moum et al. 1995) or an identified turbulent patch (Moum 1996). This
128 effectively produces one value of dissipation or diffusivity for a given depth interval. Similarly,
129 the Thorpe-scale method requires the calculation of the root-mean-square (*rms*) displacement scale
130 with respect to a finite depth window. In section 3d we will apply the Osborn, Osborn-Cox, and
131 Thorpe-scale methods to quantities calculated from vertical profiles extracted from the DNS.

132 Turbulence in strongly stratified fluids is often highly intermittent in space and time (see e.g.
 133 Rorai et al. (2014); Portwood et al. (2016)). This raises the following question: how well can a
 134 limited set of observations reproduce the volumetrically-averaged turbulent diffusivity? In section
 135 3d, we will also address this question by calculating the turbulent diffusivity with a limited number
 136 of vertical profiles extracted from the DNS. This can be interpreted as a best case scenario for
 137 observations of turbulent mixing without any measurement errors. In section 4, we discuss our
 138 results, and draw some conclusions.

139 **2. Simulation setup and methodology**

140 *a. Governing Equations*

141 The objective of the DNS is to simulate stratified turbulence in a quasi-equilibrated state where
 142 the energy input from large-scale forcing is balanced by small-scale dissipation and mixing. The
 143 simulations solve the non-hydrostatic Boussinesq equations that can be written in non-dimensional
 144 form normalized by a characteristic velocity scale, U , length scale, L , and background buoyancy
 145 frequency, N_0 . The non-dimensional equations are

$$\nabla \cdot \mathbf{u} = 0 \quad (2a)$$

$$\frac{\partial \mathbf{u}}{\partial t} + \mathbf{u} \cdot \nabla \mathbf{u} = - \left(\frac{1}{\text{Fr}} \right)^2 \rho \hat{\mathbf{z}} - \nabla p + \frac{1}{\text{Re}} \nabla^2 \mathbf{u} + \mathcal{F} \quad (2b)$$

$$\frac{\partial b}{\partial t} + \mathbf{u} \cdot \nabla b + w = \frac{1}{\text{RePr}} \nabla^2 b, \quad (2c)$$

148 where the nondimensional parameters are a characteristic Froude number, the Prandtl number and
 149 a characteristic Reynolds number, defined as

$$\text{Fr} \equiv \frac{U}{N_0 L}, \quad \text{Pr} \equiv \frac{\nu}{\kappa_m} \quad \text{and} \quad \text{Re} \equiv \frac{UL}{\nu}.$$

150 Note that the diffusion of the scalar is specified by a characteristic Péclet number $Pe \equiv UL/\kappa_m =$
151 $RePr$. The buoyancy, $b \equiv -g\rho/\rho_0$ can be related to temperature through a linear equation of state,
152 $b = \alpha g(T - T_0)$ where ρ_0 and T_0 are reference density and temperature and α is the thermal ex-
153 pansion coefficient. Note that b in Eq. 2c is defined as the departure from an imposed background
154 gradient such that the total buoyancy is $b_T = b + N_0^2 z$. Periodic boundary conditions are then ap-
155 plied to b . In effect, this maintains a constant buoyancy difference between the top and bottom of
156 the computational domain.

157 *b. Numerical methods*

158 Equations (2) are solved in a triply periodic domain with the pseudospectral technique discussed
159 in Almalkie and de Bruyn Kops (2012b). Spatial derivatives are computed in Fourier space, the
160 nonlinear terms are computed in real space, and the solution is advanced in time in Fourier space
161 with the variable-step, third-order, Adams-Bashforth algorithm with pressure projection. The non-
162 linear term in the momentum equation is computed in rotational form, and the advective term in
163 the internal energy equation is computed in conservation and advective forms on alternate time
164 steps. These techniques are standard to ensure conservation of energy and to eliminate most alias-
165 ing errors, but the simulations reported in this paper are fully de-aliased in accordance with the 2/3
166 rule via a spectral cutoff filter.

167 The body force \mathcal{F} in (2) is implemented using the deterministic forcing schema denoted Rf
168 in Rao and de Bruyn Kops (2011). The objective is to force all the simulations to have the same
169 spectra $E_h(\kappa_h, \kappa_z)$ with $\kappa_h < \kappa_f$ and $\kappa_z = 0$. E_h is the power spectrum of the horizontal contribution
170 to kinetic energy averaged over annuli of constant horizontal wave number κ_h and vertical wave
171 number κ_z . The highest wave number forced is $\kappa_f = 16\pi/L_h$, with L_h the horizontal dimension of
172 the numerical domain. Deterministic forcing requires choosing a target spectrum $E_f(\kappa_h < \kappa_f, 0)$.

173 In contrast to turbulence that is isotropic and homogeneous in three dimensions, there are no
 174 theoretical model spectra for E_f (c.f. (Overholt and Pope 1998)). Therefore, run 2 from Lindborg
 175 (2006) was rerun using a stochastic forcing schema similar to that used by Lindborg and denoted
 176 schema Qg in Rao and de Bruyn Kops (2011). The spectrum for $E_h(\kappa_h < \kappa_f, 0)$ was computed
 177 from this simulation and used as the target for the simulations reported in the current paper.

178 In addition to forcing the large horizontal scales, 1% of the forcing energy is applied stochas-
 179 tically to the horizontal velocity components through wave number modes with $\kappa_h = 0$ and
 180 $\kappa_z = 2\pi j/L_v$, $j = 2, 3, 4$. Here L_v is the vertical dimension of the numerical domain. This random
 181 forcing induces some vertical shear (Lindborg 2006). There is no forcing of the vertical velocity
 182 in the simulations.

183 The extent of the domain in the horizontal and vertical directions are L_h and L_v with L_h/L_v
 184 chosen to accommodate the vertical motions that develop in the flow. While the simulation do-
 185 mains are not cubes and the vertical extent of the domain varies with the chosen characteristic
 186 Froude number, the grid spacing Δ is the same in all directions. It is assumed for the purpose
 187 of choosing the resolution of the numerical grid that the flows are approximately isotropic at
 188 the smallest length scales in the simulation. Therefore, a three-dimensional grid with spacing
 189 $\Delta = L_h/N_x = L_h/N_y = L_v/N_z$ with N_x , N_y , and N_z being the number of grid points in the x , y , and
 190 z directions, respectively, is used and any small-scale anisotropy in the flows can be attributed to
 191 flow physics rather than to numerical artifacts of an anisotropic grid (c.f. Waite (2011)).

192 *c. Parameters*

193 Three simulations (labeled A, B and C) are analyzed here, and the related non-dimensional pa-
 194 rameters are listed in Table 1. In each case the non-dimensional horizontal domain size is 2π .
 195 Simulations A and B have the same characteristic Froude number, $Fr = 0.0416$, representing

196 relatively strong stratification. The Reynolds number is larger in Simulation A compared to Simu-
 197 lation B. Simulation C has a moderate Reynolds number and a larger characteristic Froude number
 198 representing weaker stratification.

199 Equations (2) are time-stepped until a statistically steady state is reached. The simulations can be
 200 described using non-dimensional parameters derived using turbulent properties in the final state.
 201 For this purpose it is useful to define the turbulent kinetic energy (TKE) $k \equiv \langle \mathbf{u}' \cdot \mathbf{u}' \rangle_V^{1/2} / 2$ and the
 202 TKE dissipation rate $\langle \varepsilon \rangle_V \equiv 2\nu \langle s_{ij}s_{ij} \rangle_V$, where

$$s_{ij} \equiv \frac{1}{2} \left(\frac{\partial u'_i}{\partial x_j} + \frac{\partial u'_j}{\partial x_i} \right) \quad (3)$$

203 is the fluctuating rate of strain tensor, $\langle \cdot \rangle_V$ denotes an average over the computational domain and
 204 primes denote departures from this volume average. The Reynolds number of the turbulent flow
 205 can then be characterized using the horizontal *rms* velocity, $u_{rms} \equiv \langle \mathbf{u}'_h \cdot \mathbf{u}'_h \rangle_V^{1/2}$ and a characteristic
 206 length scale. Two choices for the length scale are the integral length scale, L_h , and the turbulent
 207 length scale, $L_t \equiv \langle k \rangle_V^{3/2} / \langle \varepsilon \rangle_V$, thereby forming two derived Reynolds numbers,

$$Re_h \equiv \frac{u_{rms} L_h}{\nu}, \quad \text{and} \quad Re_t \equiv \frac{u_{rms} L_t}{\nu}. \quad (4)$$

208 Here L_h is computed from the longitudinal horizontal velocity spectra using the method of Comte-
 209 Bellot and Corrsin (1971) (see their Appendix E). Similarly, the relative strength of stratification
 210 can be quantified by two derived Froude numbers,

$$Fr_h \equiv \frac{u_{rms}}{N_0 L_h}, \quad \text{and} \quad Fr_t \equiv \frac{u_{rms}}{N_0 L_t}. \quad (5)$$

211 The integral scale L_h is a direct estimate of the length scale of the motions responsible for most
 212 of the kinetic energy in a flow. Since calculation of L_h requires two point statistics to compute,
 213 L_t has long been used as a surrogate, and we provide it here to facilitate comparisons with other
 214 data. For isotropic homogeneous turbulence, $\mathcal{D} \equiv L_h / L_t \approx 0.5$ (Pope 2000), and for decaying

unstratified turbulence it has been observed to be as high as 1.81 (Sreenivasan 1998; Wang et al. 1996). For stratified turbulence with unity Pr , \mathscr{D} ranges from 0.3 to 0.5 (de Bruyn Kops 2015; Maffioli and Davidson 2016) and decreases with decreasing buoyancy Reynolds number (defined in the next paragraph) (de Bruyn Kops and Riley 2019). In the current simulations with $Pr = 7$, \mathscr{D} is approximately 0.1.

Stratification and viscosity can both act to inhibit turbulence motions. The combination of these effects can be quantified using a buoyancy Reynolds number (also referred to as a turbulent activity coefficient Dillon and Caldwell (1980); Gibson (1980)),

$$Re_B \equiv \frac{\langle \varepsilon \rangle_V}{\nu N_0^2}. \quad (6)$$

From this definition, the buoyancy Reynolds number can be related to a ratio of Ozmidov and Kolmogorov scales, $Re_B = (L_O^V/L_K^V)^{4/3}$, where

$$L_K^V \equiv \left(\frac{\nu^3}{\langle \varepsilon \rangle_V} \right)^{1/4}, \quad \text{and} \quad L_O^V \equiv \frac{\langle \varepsilon \rangle_V^{1/2}}{N_0^3}. \quad (7)$$

Loosely, the Ozmidov scale characterizes the size of the largest turbulent overturns permitted by stratification and the Kolmogorov scale characterizes the size of the smallest motions permitted by viscosity. Therefore, Re_B provides a measure of the dynamic range associated with turbulent overturning motions, largely unaffected by either buoyancy or viscosity. The simulations in Table 1 are listed in order of increasing Re_B . Values of Re_B in this range are common in the ocean interior according to a recent estimate based on ARGO data (Salehipour et al. 2016) and fine-scale parameterizations (Gregg 1989b). Larger values of Re_B are also observed (Moum 1996), but these are not currently accessible with DNS of strongly stratified flows with realistic Pr .

For comparison with observations it is useful to construct a set of dimensional parameters for each simulation. Here, this is done by setting the dimensional vertical domain size to 5m and the kinematic viscosity to $10^{-6} \text{m}^2 \text{s}^{-1}$, appropriate for water. The dimensional domain size was

chosen to match roughly the size of typical turbulent patches in the ocean interior and the vertical size typically used for averaging microstructure measurements. Once the dimensional domain size and kinematic viscosity are set, the dimensional time scale can be found from the characteristic Reynolds number, Re . Some of the dimensional parameters are listed in Table 2. The dimensional values of the background buoyancy frequency, N_0 , are in the range $3.7 \times 10^{-3} \text{s}^{-1}$ to $1.4 \times 10^{-2} \text{s}^{-1}$, corresponding to buoyancy periods ranging from 28.0 to 7.4 min. The weakest stratification considered here is within the range observed by Moum (1996) in the main thermocline while the strongest stratification considered here is more typical of the seasonal pycnocline (e.g. Alford and Pinkel (2000)). The dimensional average turbulent dissipation rate spans more than two orders of magnitude and contains values typically measured in the ocean interior (e.g. Moum (1996); Gregg (1989b)).

3. Results

a. Vertical section and profiles

Turbulence and mixing are intermittent across a wide range of scales in the DNS. On small scales, the statistics of energy and buoyancy variance dissipation are skewed with a small number of large events dominating the volume average. This is a well-known property of high Reynolds number turbulence in unstratified flows (Sreenivasan and Antonia 1997) and intermittency in scalar mixing is discussed extensively in Warhaft (2000). On larger scales, turbulence occurs in localized bursts separated by relatively quiescent flow. Similar behavior has been observed in numerous previous studies (e.g. Riley and de Bruyn Kops (2003); Hebert and de Bruyn Kops (2006a); Rorai et al. (2014); Portwood et al. (2016)).

Figure 1 shows vertical slices of the buoyancy b , TKE dissipation rate ε , and the buoyancy flux $B = w'b'$, extracted from Simulation C. The other simulations (not shown) have qualitatively similar features. Here, buoyancy is normalized by the background stratification, while ε and B are normalized by their volume averages.

A series of distinct layers are visible in the buoyancy field (top row) with relatively thick weakly stratified regions separated by relatively thin and more strongly stratified interfaces. The turbulent dissipation rate (middle row) exhibits localized patches of strong turbulence similar to those described in Portwood et al. (2016). Maximum local values of ε are up to 30 times larger than the volume average. The turbulent buoyancy flux (bottom row) also exhibits large fluctuations with peak values up to 50 times larger than the volume average. Regions with large positive values of B often occur next to regions with large negative values, reflecting vertical displacements of the isopycnals (e.g. compare lower right and upper right panels).

Statistics collected along a single vertical profile corresponding to the white dashed line in Figure 1 are shown in Figure 2. The red dashed line in Figure 2(a) shows the 1D sorted buoyancy profile. The displacement scale L_d is the change in height of a fluid parcel from its unsorted to sorted positions. Several features in the profiles shown in Figure 2 resemble qualitatively the observed profiles reported in Moum (1996) such as the step-like structure in the density field and the corresponding structure in the Thorpe displacement scale (see, e.g. Figure 1b in Moum (1996)). To compare with the TKE dissipation rate ε it is convenient to introduce the perturbation potential energy. In a volume with constant background buoyancy gradient N_0^2 , the perturbation potential energy is $\langle b'^2 \rangle_V / (2N_0^2)$ and its associated dissipation rate can be written

$$\chi \equiv \frac{\kappa_m \nabla b' \cdot \nabla b'}{N_0^2}. \quad (8)$$

278 A profile of χ , normalized by its volume average is shown in Figure 2(e). Since N_0^2 is constant
 279 in our simulations, χ is proportional to the dissipation rate of buoyancy variance, and hence is
 280 a natural measure of irreversible mixing. We observe that both ε and χ are highly intermittent
 281 throughout the water column with neither obviously correlated with the density field. There is also
 282 no clear correlation between locations with large ε and χ . As a result, a local mixing efficiency,
 283 $\eta(\mathbf{x}, t)$, which may be defined as

$$\eta(\mathbf{x}, t) \equiv \frac{\chi}{\chi + \varepsilon}, \quad (9)$$

284 fluctuates rapidly between 0 and 1.

285 *b. Length scales*

286 The relative importance of stratification and viscosity to the turbulent motions at a particular
 287 scale can be quantified by comparing various length scales associated with stratified turbulence
 288 (Smyth and Moum 2000). Figure 3 shows characteristic length scales for each simulation, plotted
 289 as a function of the buoyancy Reynolds number, Re_B . Here, dimensional values are plotted, where
 290 the vertical domain size is set to 5m as discussed above.

291 In dimensional terms, the Kolmogorov scale, L_K , ranges from 2.4mm to 8.7mm, while the Batch-
 292 elor scale, $L_B = L_K / \sqrt{Pr}$ ranges from 0.9mm to 3.3mm. The isotropic grid spacing, $\Delta_{x,y,z}$ is always
 293 less than twice the Batchelor scale, ensuring that the DNS is sufficiently well-resolved. The wide
 294 scale separation between the domain size and the grid spacing gives an indication of the large
 295 computational cost of these simulations.

296 There are several different ways to construct a Thorpe scale from a three-dimensional dataset
 297 (see Smyth and Moum (2000) and Mashayek et al. (2017a) for further discussion). For example,
 298 it would be possible to sort a three-dimensional density field and then calculate the Thorpe scale
 299 from the *rms* vertical displacements with respect to the volumetrically-sorted profile. Here, moti-

300 vated by oceanographic observations where three-dimensional sorting is typically not possible, we
 301 instead vertically sort the density profile at each horizontal gridpoint. The Thorpe scale is then cal-
 302 culated from each vertical profile and the result shown in Figure 3 is averaged over all horizontal
 303 gridpoints. Specifically,

$$L_T^V \equiv \left\langle \left\langle L_d^2 \right\rangle_z^{1/2} \right\rangle_{x,y}, \quad (10)$$

304 where $\langle \cdot \rangle_z$ denotes an average in the vertical direction and $\langle \cdot \rangle_{x,y}$ denotes an average in the horizon-
 305 tal directions. Later, in section 3d, we will examine the sensitivity of the Thorpe scale estimates
 306 calculated with a limited number of vertical profiles.

307 The dimensional Thorpe and Ozmidov scales calculated using volumetric simulation data, L_T^V
 308 and L_O^V are both $\simeq 10\text{cm}$ and increase somewhat with increasing buoyancy Reynolds number.
 309 The Ozmidov scale increases with Re_B faster than the Thorpe scale such that the ratio L_O^V/L_T^V is
 310 0.53 in simulation A, 0.56 in simulation B, and 0.92 in simulation C. This can be compared with
 311 $L_O/L_T \simeq 0.8$ suggested by Dillon and Caldwell (1980). The dependence of this ratio on the flow
 312 parameters is consistent with the recent conclusions of Mater et al. (2015) and Scotti (2015).

313 *c. Testing of Osborn, Osborn-Cox, and Dillon methods*

314 In this section, we will compare the vertical turbulent diffusivity diagnosed directly from the
 315 simulations with values inferred from the Osborn, Osborn-Cox, and Dillon methods. Before giving
 316 the results, a brief description of each method is given below, highlighting in particular some of
 317 the key assumptions behind each method.

318 1) OSBORN-COX METHOD

319 Starting from an equation for entropy density, Osborn and Cox (1972) derived a method to
 320 estimate the vertical turbulent diffusivity from measurements of microscale temperature or con-

ductivity. Here, we will write the equations in terms of buoyancy b with the understanding that this is more closely related to temperature than salinity since the Prandtl number is 7 in the DNS. The buoyancy variance budget (as noted above this is linearly related to the perturbation potential energy in this context) can be written as

$$\left(\frac{\partial}{\partial t} + \langle \mathbf{u} \rangle \cdot \nabla \right) \langle b'^2 \rangle + \nabla \cdot (\langle \mathbf{u} b'^2 \rangle - \kappa_m \nabla \langle b'^2 \rangle) = -2 \langle \mathbf{u} b' \rangle \cdot \nabla \langle b \rangle - 2 \kappa_m \langle \nabla b' \cdot \nabla b' \rangle, \quad (11)$$

where angle brackets denote an average over some arbitrary volume (e.g. Pope (2001)). Assuming that terms on the left hand side, the time rate of change and flux of buoyancy variance, are both small, Eq. 11 reduces to a production-dissipation balance

$$- \langle \mathbf{u}' b' \rangle \cdot \nabla \langle b \rangle = \kappa_m \langle \nabla b' \cdot \nabla b' \rangle = \langle \chi \rangle \langle N^2 \rangle, \quad (12)$$

using Eq. 8. Further neglecting the horizontal buoyancy flux and defining the vertical diffusivity in terms of these (arbitrary) volume average, i.e. $\kappa \equiv - \langle B \rangle / \langle N^2 \rangle$ yields an estimate of the vertical turbulent diffusivity,

$$\kappa_{O-C} \equiv \frac{- \langle B \rangle}{\langle N^2 \rangle} \simeq \frac{\langle \chi \rangle}{\langle N^2 \rangle}. \quad (13)$$

2) OSBORN METHOD

The Osborn method (Osborn 1980) provides a way to estimate the vertical diffusivity associated with small-scale turbulence from the TKE dissipation rate. In deriving the method, Osborn made several key assumptions (see e.g. Mashayek et al. (2013) for further discussion), including that the vertical diffusivity is dominated by fully developed turbulence, and that the turbulence exhibits a quasi-steady balance between production, dissipation and diapycnal mixing *when suitably averaged* so that the mixing can be related to the dissipation rate. Therefore, the TKE budget reduces to a balance between production, buoyancy flux, and dissipation, (with crucially no contribution

340 from advective or boundary processes) i.e.

$$\langle P \rangle = \langle \varepsilon \rangle - \langle B \rangle, \quad (14)$$

341 where

$$\langle P \rangle \equiv - \langle u'_i u'_j \rangle \frac{\partial \langle u_i \rangle}{\partial x_j} \quad (15)$$

342 is the turbulent shear production and

$$B \equiv w' b' \quad (16)$$

343 is the buoyancy flux. Osborn (1980) further assumed that small-scale turbulence is isotropic so that
 344 the dissipation rate can be determined from just one component of the deformation rate tensor. We
 345 do not test this assumption here and instead evaluate the production and dissipation using the full
 346 deformation rate tensor. The appropriateness of the assumption of small-scale isotropy for strat-
 347 ified turbulence has been discussed extensively in recent papers (e.g. Hebert and de Bruyn Kops
 348 (2006b); Almalkie and de Bruyn Kops (2012a); de Bruyn Kops (2015)). Osborn (1980) further
 349 suggested that the assumption of quasi-steadiness and hence the averaging operator could be ap-
 350 plied to vertical profiles through turbulent patches ranging from 1-10m in size. These assumptions
 351 then imply that the flux Richardson number, $R_f \equiv - \langle B \rangle / \langle P \rangle$ (or $R_f = \langle B \rangle / (\langle B \rangle - \langle \varepsilon \rangle)$ using Eq.
 352 (14)) is constant. Using this definition and Eq. 14 implies that the buoyancy flux is

$$\langle B \rangle = - \left(\frac{R_f}{1 - R_f} \right) \langle \varepsilon \rangle. \quad (17)$$

353 Then, the vertical turbulent diffusivity, $\kappa = - \langle B \rangle / \langle N^2 \rangle$, can be related to the TKE dissipation
 354 rate ε to yield the estimate

$$\kappa_O = \Gamma \frac{\langle \varepsilon \rangle}{\langle N^2 \rangle}, \quad (18)$$

355 where $\Gamma \equiv \left(\frac{R_f}{1 - R_f} \right)$. This turbulent flux coefficient Γ is often referred to as a ‘mixing efficiency’,
 356 although in principle it can be greater than one, and there has been much recent activity attempting

357 to produce appropriate parameterizations for this quantity in terms of various flow parameters, see
 358 for example Salehipour et al. (2016); Mashayek et al. (2017b); Monismith et al. (2018).

359 3) THORPE-SCALE METHOD

360 Thorpe (1977) proposed a method to estimate the averaged dissipation rate based on vertical
 361 profiles of potential density. An advantage of this method is that it can be applied to more readily
 362 available data, allowing, for example, the generation of global maps of dissipation (e.g. Water-
 363 house et al. (2014)). To calculate the Thorpe scale, a density profile is first sorted so that the sorted
 364 density is a monotonic function of height. The Thorpe displacement length L_d is the difference in
 365 height of a water parcel from its unsorted to sorted location (figure 2(c)). The Thorpe length scale
 366 is then calculated by taking the root mean square of L_d , i.e.

$$L_T^P = \langle L_d^2 \rangle_P^{1/2}, \quad (19)$$

367 where angle brackets are typically taken to represent an appropriate ‘patch’ average, for example
 368 taken over a single overturning turbulent patch or an ensemble of such patches obtained from
 369 vertical profiling instruments (Thorpe 2005). Thorpe (1977) conjectured that L_T may be linearly
 370 related to the Ozmidov scale calculated with patch-averaged quantities, $L_O^P = \langle \varepsilon \rangle_P^{1/2} \langle N^2 \rangle_P^{-3/2}$.
 371 This then gives an estimate of the dissipation rate

$$\langle \varepsilon \rangle_P = R_{OT}^2 (L_T^P)^2 \langle N^2 \rangle_P^{3/2}, \quad (20)$$

372 where the coefficient of proportionality, $L_O^P/L_T^P \equiv R_{OT} \simeq 0.8$, is based on observations by Dillon
 373 and Caldwell (1980), although there is mounting evidence that estimates of this coefficient can be
 374 both biased and uncertain (Mater et al. 2015; Scotti 2015; Mashayek et al. 2017a). Then, using
 375 Eq. 18 yields an estimate for the vertical turbulent diffusivity,

$$\kappa_T = 0.64 \Gamma (L_T^P)^2 \langle N^2 \rangle_P^{1/2}. \quad (21)$$

376 4) COMPARISON

377 The underlying assumptions behind the three methods described above are questionable in
 378 strongly stratified flows where turbulent events are highly intermittent in time and space as il-
 379 lustrated in Figure 1. This concern becomes stronger when a small subset of the flow is sampled,
 380 for example using a small number of vertical profiles, as the various averages being taken become
 381 less reliable as representative of turbulent mixing events within the flow. Before addressing the
 382 issue of incomplete sampling and averaging, we will first examine the performance of the ap-
 383 proximate methods described above, compared with the ‘direct’ calculation of κ formed using the
 384 volume-averaged buoyancy flux and stratification, i.e.

$$\kappa_d^V = \frac{-\langle B \rangle_V}{\langle N^2 \rangle_V}. \quad (22)$$

385 When calculated using data from the full computational volume, the vertical turbulent diffusivity
 386 associated with the Osborn-Cox, Osborn, and Thorpe methods can be written

$$\kappa_{O-C}^V = \frac{\langle \chi \rangle_V}{\langle N^2 \rangle_V}, \quad \kappa_O^V = \Gamma \frac{\langle \varepsilon \rangle_V}{\langle N^2 \rangle_V}, \quad \kappa_T^V = 0.64 \Gamma (L_T^V)^2 \langle N^2 \rangle_V^{1/2}, \quad (23)$$

387 respectively, where $\langle \cdot \rangle_V$ denotes an average over the full computational volume and L_T^V is de-
 388 fined in Eq. 10. Figure 4 shows κ_{O-C}^V , κ_O^V and κ_T^V , normalized by κ_d^V as defined in Eq. 22 and
 389 plotted against the buoyancy Reynolds number to differentiate the three simulations. The dimen-
 390 sional values of κ_d^V are $2.2 \times 10^{-6} \text{m}^2 \text{s}^{-1}$ in Simulation A, $1.8 \times 10^{-5} \text{m}^2 \text{s}^{-1}$ in Simulation B, and
 391 $7.2 \times 10^{-5} \text{m}^2 \text{s}^{-1}$ in Simulation C, roughly spanning typical values found in the ocean interior
 392 (Waterhouse et al. 2014).

393 Even with perfect sampling of the 3D volume, there is significant scatter between the various
 394 estimates of κ . The estimates using the Osborn and Osborn-Cox methods, κ_O^V and κ_{O-C}^V are within
 395 40% of κ_d^V , and there is no clear trend with Re_B . The Thorpe-scale method underestimates κ_d^V by
 396 about 50% in Simulation C, but significantly overestimates κ_d^V in Simulations A and B.

397 When the Thorpe scale is small and/or when the density contrast is weak, it can be difficult to
398 distinguish between real overturns and measurement error associated with a CTD profile (Klymak
399 and Nash 2007; Johnson and Garrett 2004). In simulation A, for example, the dimensional Thorpe
400 scale is $\sim 11\text{cm}$. If some of the overturns are too small or weak to be measured from a CTD
401 profile(s), the Thorpe scale inferred from these observations could be underestimated. It is possible
402 that this sampling error could partially compensate for an overestimate of κ derived from the
403 Thorpe-scale method.

404 *d. Vertical profile-averaged statistics*

405 The estimates of the vertical turbulent diffusivity described above were calculated using simu-
406 lation data extracted from the full three-dimensional volume. In contrast, data collected from the
407 ocean are necessarily much more limited. In this section, we explore the sensitivity of the esti-
408 mates of κ when calculated with limited data. Note that we do not consider instrument error or
409 biases introduced when converting measured quantities into physical quantities like the dissipa-
410 tion rate. Instead, we assume that the simulated field can be sampled perfectly at discrete points
411 in space and focus on the influence of limited data availability.

412 The most common sampling strategy to infer κ is to collect velocity, temperature and/or con-
413 ductivity along roughly vertical profiles. Measurements from distinct regions within one or more
414 profiles are often averaged to reduce the uncertainty in the measurement. Here, we will calculate
415 κ using the methods described in the previous section based on a limited number of 1D vertical
416 profiles extracted from the simulations. Note that the profiles that we use are taken instantaneously
417 and are perfectly vertical. How well this describes oceanographic measurements depends on the
418 fall speed of the instrument and the speed of the currents. Some platforms such as microstructure

gliders make significantly inclined profiles, although these data are often analyzed in a similar way to free-falling profilers (e.g. Palmer et al. (2015)).

We extract data from the simulations by randomly selecting a set of vertical profiles from a single three-dimensional field. Since the simulations were sampled when the flow is in a statistically stationary state, sampling at different spatial locations should give the same statistical result as sampling at different time intervals. Treating a limited number of samples as independent vertical profiles is justified by the horizontal de-correlation of statistical quantities. For example, Figure 5 shows the horizontal autocorrelation length associated with the TKE dissipation rate $\langle \epsilon \rangle_z$, where $\langle \cdot \rangle_z$ denotes an average applied over a single vertical profile. In all cases $\langle \epsilon \rangle_z$ is de-correlated over a distance of $\sim 2L_z$ or $\sim 10\text{m}$ in the horizontal. Note that the properties of the large-scale flow in the simulations will be influenced by the forcing scheme used. In the ocean, where turbulence is associated with eddies, internal waves, and shear layers across a wide range of horizontal scales, the de-correlation distance between profile-averaged statistics could be much larger than 10m .

Before testing the methods for estimating κ it is useful to quantify the variability in profile-averaged statistics induced by intermittent stratified turbulence. Figure 6 shows the probability density function (PDF) of the buoyancy flux, TKE and potential energy dissipation rates, and squared Thorpe scale, each normalized by the corresponding volume average. Here the Thorpe scale is calculated by averaging the *rms* displacement over one vertical profile such that

$$L_T^z \equiv \langle L_d^2 \rangle_z^{1/2}. \quad (24)$$

Each PDF is calculated using the full 3D computational volume (i.e. vertical profiles were collected at every horizontal gridpoint). The Thorpe scale is squared for comparison with the other quantities since this quantity appears in the expression for κ_T .

440 The modes of the PDFs for all quantities shown in Figure 6 are skewed towards values smaller
 441 than the volume average. It is well known in the turbulence literature that the point-wise TKE
 442 and variance dissipation rates are similarly skewed such that a small number of large values con-
 443 tribute significantly to the volume average Pope (2000). The PDFs of local (pointwise) ε and
 444 χ are typically assumed to be lognormal, following Kolmogorov (1962). de Bruyn Kops (2015)
 445 shows that distributions of local ε and χ in stratified turbulence are well-approximated by the
 446 lognormal model provided that $Re_b > O(10)$. For lower Re_b , the multiple turbulence regimes de-
 447 scribed by Portwood et al. (2016) result in differences in the distributions that are evident in plots
 448 on logarithmic axes but are not visible in Figure 6. The TKE dissipation rate measured in the
 449 ocean thermocline is similarly skewed (Baker and Gibson 1987; Gregg et al. 1996). Evidently the
 450 intermittency inherent in the point-wise statistics extends to the profile-averaged statistics.

451 Here, we calculate ε and χ using derivatives of all three velocity components and buoyancy in
 452 all three spatial directions. Field measurements of these quantities generally involve a subset of the
 453 velocity and/or gradient information and assumptions about the isotropy of the small-scale turbu-
 454 lence are invoked to fill in the missing information. The PDFs of the surrogates for ε and χ based
 455 on a subset of the velocity and scalar gradients are significantly different from those of the exact
 456 quantities. In particular, the left side of the distributions of the surrogates tend toward exponential
 457 (Almalkie and de Bruyn Kops 2012a; de Bruyn Kops 2015) and the mean of the surrogates are
 458 significantly different from the exact values when Re_b is low (Hebert and de Bruyn Kops 2006b).

459 The variance associated with the buoyancy flux is much larger than the variance in other quan-
 460 tities. This appears to be associated with a large contribution from internal waves. Figures 1 and
 461 2 show patches of alternating sign of $w'b'$, indicating reversible transfers between kinetic and po-
 462 tential energy (note that Figure 6 only shows positive values of the normalized buoyancy flux).

As we will see below, the large variability in the profile-averaged buoyancy flux has significant implications for the estimates of κ .

Figure 7 shows a PDF of the mixing efficiency calculated using the profile-averaged dissipation rates, i.e. $\langle \chi \rangle_z / (\langle \chi \rangle_z + \langle \varepsilon \rangle_z)$, which exhibits significant scatter about the volume average. The mean and mode of the distributions increase from Simulation A to Simulation C as the buoyancy Reynolds number increases. The mean values (dashed lines) are somewhat larger than the canonical value of $1/6$, ranging from 0.18 in Simulation A to 0.28 in simulation C, although the spread about the mean is considerable. For example $\sim 22\%$ of the profiles taken from Simulation C have a mixing efficiency larger than 0.4, although such large values do arise in idealised flows subject to strong Kelvin-Helmoltz-like shear-driven overturning motions (see for example Mashayek et al. (2013, 2017a)).

The estimates of the vertical diffusivity calculated using sets of randomly selected vertical profiles are shown in Figure 8. Specifically, when applied to n vertical profiles, the vertical diffusivity estimated from the Osborn-Cox, Osborn, and Thorpe methods can be written

$$\kappa_{O-C}^{z,n} = \frac{\langle \chi \rangle_{z,n}}{\langle N^2 \rangle_{z,n}}, \quad \kappa_O^{z,n} = \Gamma \frac{\langle \varepsilon \rangle_{z,n}}{\langle N^2 \rangle_{z,n}}, \quad \kappa_T^{z,n} = 0.64 \Gamma (\langle L_T^z \rangle_n)^2 \langle N^2 \rangle_{z,n}^{1/2}, \quad (25)$$

respectively, where $\langle \cdot \rangle_{z,n}$ denotes an average over n vertical profiles and L_T^z is defined in Eq. (24).

Similarly, the vertical diffusivity associated with the direct method applied to n vertical profiles is

$$\kappa_d^{z,n} = \frac{-\langle B \rangle_{z,n}}{\langle N^2 \rangle_{z,n}}. \quad (26)$$

Note that here $\langle N^2 \rangle_{z,n} = N_0^2$ due to the periodicity of the computational domain. In Figure 8 each estimate of κ is dimensionalized such that the height of the vertical domain and the length of each profile is 5m. Solid colored lines show ± 1 standard deviation about the mean and the area between these curves is shaded to highlight the uncertainty associated with each estimate. Black dashed lines indicate the vertical diffusivity calculated with the volume-averaged buoyancy flux,

484 i.e. κ_d^V . In some practical cases, a longer section of a vertical profile might be used to estimate κ .
 485 For reference, Figure 8 also indicates the total dimensional vertical distance used in the averaging.
 486 Here, the average of 20 profiles of 5m each can be compared with the average across a single 100m
 487 profile, with the caveat that the profiles in our simulations are not contiguous.

488 In all cases, $\kappa_d^{z,n}$ converges very slowly to κ_d^V . Figure 9 shows the standard deviation of the
 489 averages of the buoyancy flux, kinetic and potential energy dissipation rates, and the squared
 490 Thorpe scale for a given number of vertical profiles. In all cases the standard deviation decreases
 491 with the square root of the number of profiles (compare with dashed line) as expected from the
 492 central limit theorem for independent random variables. However, even with 20 profiles, negative
 493 values of $\kappa_d^{z,n}$ are within one standard deviation of the mean in Simulations A and B. The variance
 494 is smaller in Simulation C where the flow is more turbulent.

495 The standard deviation associated with the profile-averaged dissipation rate and Thorpe scales
 496 are much smaller than the standard deviation of the buoyancy flux in Simulations A and B. As
 497 seen in Figure 4, the Osborn and Osborn-Cox methods give a relatively good estimate of κ_d^V
 498 in these cases. Interestingly, the standard deviations of $\langle \epsilon \rangle_{z,n}$ and $\langle \chi \rangle_{z,n}$ are significantly larger
 499 in Simulation C and as a result the Osborn and Osborn-Cox methods require more profiles to
 500 converge in this case. Since Simulation C is the most turbulent, having the largest dissipation rate,
 501 diffusivity, and buoyancy Reynolds number, the slow convergence of the Osborn and Osborn-
 502 Cox methods is unexpected and an explanation for this behavior is not immediately clear. In
 503 comparison, the Thorpe-scale method converges relatively quickly in Simulation C.

504 *e. Validity of assumptions underlying the Osborn method*

505 Remarkably, when applied to a limited number of vertical profiles, in terms of the relative error
 506 the Osborn method, using (18), performs quite well, due apparently to compensating errors in two

of its constituent parts. Figure 10 shows the fractional error associated with the classic Osborn relation (Eq. 18, blue curve), the assumption that the turbulent flux coefficient Γ is constant (green curve), and the assumed quasi-steady balance (unaffected by advection) in the TKE budget (Eq. 14, red curve). Here, the fractional error is defined as the absolute value of the sum of the terms in each relation (with all terms on one side of the relevant equation) divided by the sum of the absolute values of each individual term. The vertical and profile average is not shown in the legend for notational clarity but is applied to ε , B , P , and N^2 individually.

One might expect the error associated with the Osborn relation (18) to be at least as large as that of the worst assumed component underlying the relation. Instead, the error associated with the Osborn relation is significantly less than the errors associated with the equations for the flux coefficient and TKE budgets for Simulations A and B. In case C the error in the Osborn relation is comparable to the error associated with the error associated with the flux coefficient and smaller than the error associated with the TKE budget.

An important difference between the Osborn relation and the equations for the flux coefficient and the TKE budget is that the buoyancy flux appears in the latter two relations but does not appear explicitly in the Osborn relation. Figure 8 showed that the buoyancy flux exhibits very large scatter about its mean value, and this is particularly true in Simulations A and B. One explanation for the relatively low error associated with the Osborn method is that it is not influenced by the reversible contributions of internal waves to the buoyancy flux than the equation for the flux coefficient and the TKE budget. Indeed, central to the averaging at the heart of the Osborn method is the assumption that reversible processes in the buoyancy flux are filtered out, leaving only the irreversible component, capturing the actual mixing occurring within the flow.

Relatively recently, Salehipour and Peltier (2015) proposed a ‘generalized Osborn relation’ using the framework introduced by Winters and D’Asaro (1996), designed explicitly to identify, as

531 a function of time, the diapycnal diffusivity in terms of an appropriate definition for an inherently
 532 irreversible mixing efficiency. They showed that the diapycnal diffusivity κ_p can be written as

$$\kappa_p = \frac{\mathcal{E}}{1 - \mathcal{E}} \frac{\varepsilon}{N_*^2}, \quad (27)$$

533 where \mathcal{E} is the *irreversible* and instantaneous mixing efficiency defined in Caulfield and Peltier
 534 (2000) and N_* is the buoyancy frequency calculated using the sorted density profile. Since this
 535 expression relies on quantities calculated from (volume) sorted data, it is a global measure of the
 536 mixing within the entire domain under consideration, but can in principle be calculated at every
 537 time instant within a temporally evolving flow. As the key parameters (such as an appropriately
 538 defined buoyancy Reynolds number and Richardson number) describing their simulated flow also
 539 vary in time, the results of their simulations, showing temporal variation of \mathcal{E} can be interpreted as
 540 evidence that \mathcal{E} depends on such parameters (Salehipour and Peltier 2015; Salehipour et al. 2016).
 541 Importantly, Eq. (27) does not rely on any assumptions aside from the Boussinesq approximation.

542 Salehipour and Peltier (2015) noted the clear structural similarity between Eq. (27) and the Os-
 543 born relation, Eq. (18). For strongly stratified flows with relatively small isopycnal displacements
 544 one might anticipate that the globally sorted buoyancy frequency $N_* \simeq N$. To the extent that the
 545 flux coefficient Γ in Eq. (18) approximates the irreversible flux coefficient $\mathcal{E}/(1 - \mathcal{E})$, the Osborn
 546 relation could then provide a relatively robust approximation to the diapycnal diffusivity. Funda-
 547 mentally, the key point is that assuming that the *irreversible* mixing rate is some fraction of the
 548 turbulent dissipation rate appears to be a reasonable assumption.

549 Loosely, the irreversible conversion of kinetic energy in the large-scale flow into internal energy
 550 by viscous dissipation in a stratified fluid is ‘taxed’, with approximately 20% having to be ‘spent’
 551 to increase the background potential energy due to irreversible mixing processes. This partition-
 552 ing of irreversible energetic conversion rates seems to be supported empirically, at least within the

flow considered here, even when the theoretical arguments and assumptions presented by Osborn to justify this partitioning are not satisfied, not least due to the contaminating effects of *reversible* processes. (It is important to remember in transient mixing events the approximately 20% ‘taxation’ can be substantially exceeded.) This apparently robust partitioning might help explain why the Osborn method, applied using a limited number of vertical profiles, appears to be less prone to errors introduced by the presence of internal waves and other reversible processes than the clear, and significant failure of its underlying assumptions might suggest.

4. Conclusions and discussion

In this paper we tested the performance of the Osborn, Osborn-Cox, and Thorpe-scale methods using high resolution direct numerical simulations (DNS). The simulations used an idealized triply periodic computational domain with an imposed background stratification. Turbulence was forced using a deterministic body force added to the momentum equations. The simulations can be viewed as a model of turbulence in a small region embedded within the thermocline. Three simulations were run with varying stratification and turbulence levels, typical of conditions in the main and seasonal thermoclines.

When the Osborn and Osborn-Cox methods are applied to the volume-averaged TKE and perturbation potential energy dissipation rate, the resulting estimates of the vertical turbulent diffusivity (κ_O^V and κ_{O-C}^V are within 40% of the value obtained directly from the volume-averaged turbulent buoyancy flux, κ_d^V). When the Thorpe scale is calculated using individual vertical profiles and then averaged over the full computational domain, the resulting estimate, κ_T^V is very close to κ_O^V in Simulation C but significantly overestimates κ_d^V in Simulations A and B with relatively small Re_B . In Simulation A, κ_T^V is more than 2.5 times larger than κ_d^V .

575 Consistent with previous simulations of forced stratified turbulence, we find that turbulence
576 is inherently patchy and intermittent. For example, the PDFs of the dissipation rates of kinetic
577 energy and buoyancy variance are skewed with a small number of very intense events, associated
578 with vigorous, shear-driven overturnings. We find that this intermittency extends to the statistics
579 averaged over one-dimensional vertical profiles, despite the fact that the simulations are set up
580 such that each profile has the same average stratification.

581 This finding has important implications for the interpretation of limited observational datasets
582 and for sampling strategies. For example, to ensure that the average dissipation rate can be cor-
583 rectly calculated, it would be necessary to ensure that enough of the extreme events are captured.
584 The rate at which the various estimates of κ converge to the values calculated with volume-
585 averaged statistics depends on Re_B . In general, the Osborn and Osborn-Cox methods converge
586 relatively quickly in the simulations with small values of Re_B , while the Thorpe-scale method
587 converges somewhat faster in Simulation C at larger Re_B .

588 In comparison to the Osborn and Osborn-Cox methods, the diffusivity calculated directly from
589 the vertical buoyancy flux using a small number of vertical profiles exhibits a very large scatter
590 about the mean. Remarkably in Simulations A and B, negative values of κ are within one standard
591 deviation of the average even when using 20 vertical profiles, each 5m in length. The convergence
592 to the mean is faster in Simulation C where the flow is more turbulent. The slow convergence of
593 the buoyancy flux for small Re_B appears to be due to large (and inherently reversible) contributions
594 from internal waves. In an internal wave field the sign of $w'b'$ fluctuates as energy is transferred
595 between the kinetic energy reservoir and the potential energy reservoir. A large averaging (in
596 space, in time or in ensemble) window is required to eliminate these reversible contributions to the
597 buoyancy flux, inevitably limiting the usefulness of the method in general.

598 Here, we have not tested the performance of finescale methods which rely on measurements of
599 internal waves. The large-scale forcing that was used to drive turbulence in the DNS was idealized
600 and was not necessarily intended to replicate the properties of the finescale internal wave field.
601 Simulations that simultaneously resolve a typical finescale internal wave spectrum (e.g. Gargett
602 et al. (1981)) while also resolving small-scale turbulence and mixing could be used to test (and
603 perhaps improve) finescale methods.

604 **Acknowledgements**

605 We acknowledge the support of EPSRC under the Programme Grant EP/K034529/1 ‘Mathe-
606 matical Underpinnings of Stratified Turbulence’ (MUST), and also support from the U.S. Office
607 of Naval Research under grant N00014-15-1-2248. High performance computing resources were
608 provided through the U.S. Department of Defense High Performance Computing Modernization
609 Program by the Army Engineer Research and Development Center and the Army Research Labo-
610 ratory under Frontier Project FP-CFD-FY14-007.

References

- Alford, M. H., and R. Pinkel, 2000: Observations of overturning in the thermocline: The context of ocean mixing. *J. Phys. Oceanogr.*, **30**, 805–832.
- Almalkie, S., and S. M. de Bruyn Kops, 2012a: Energy dissipation rate surrogates in incompressible Navier-Stokes turbulence. *J. Fluid Mech.*, **697**, 204–236.
- Almalkie, S., and S. M. de Bruyn Kops, 2012b: Kinetic energy dynamics in forced, homogeneous, and axisymmetric stably stratified turbulence. *J. Turbul.*, **13** (29), 1–29.
- Baker, M. A., and C. H. Gibson, 1987: Sampling turbulence in the stratified ocean: Statistical consequences of strong intermittency. *Journal of Physical Oceanography*, **17** (10), 1817–1836.
- Caulfield, C. P., and W. R. Peltier, 2000: The anatomy of the mixing transition in homogeneous and stratified free shear layers. *J. Fluid Mech.*, **413**, 1–47.
- Comte-Bellot, G., and S. Corrsin, 1971: Simple Eulerian time correlation of full and narrow-band velocity signals in grid-generated ‘isotropic’ turbulence. *J. Fluid Mech.*, **48**, 273–337.
- de Bruyn Kops, S. M., 2015: Classical turbulence scaling and intermittency in stably stratified Boussinesq turbulence. *J. Fluid Mech.*, **775**, 436–463.
- de Bruyn Kops, S. M., and J. J. Riley, 2019: The effects of stable stratification on the decay of initially isotropic homogeneous turbulence. *J. Fluid Mech.*, **860**, 787821, doi:10.1017/jfm.2018.888.
- Dillon, T. M., and D. R. Caldwell, 1980: The batchelor spectrum and dissipation in the upper ocean. *J. Geophysical Research*, **85** (C4), 1910–1916.

631 Gargett, A., P. Hendricks, T. Sanford, T. Osborn, and A. Williams, 1981: A composite spectrum
 632 of vertical shear in the upper ocean. *Journal of Physical Oceanography*, **11** (9), 1258–1271.

633 Gibson, C. H., 1980: Fossil turbulence, salinity, and vorticity turbulence in the ocean. *Marine*
 634 *Turbulence*, J. C. Nihous, Ed., Elsevier, 221–257.

635 Gregg, M., 1989a: Scaling turbulent dissipation in the thermocline. *Journal of Geophysical Re-*
 636 *search: Oceans*, **94** (C7), 9686–9698.

637 Gregg, M., 1999: Uncertainties and limitations in measuring ε and χ t. *Journal of Atmospheric*
 638 *and Oceanic Technology*, **16** (11), 1483–1490.

639 Gregg, M., E. D’Asaro, J. Riley, and E. Kunze, 2018: Mixing efficiency in the ocean. *Annual*
 640 *review of marine science*, **10**, 443–473.

641 Gregg, M., D. Winkel, T. Sanford, and H. Peters, 1996: Turbulence produced by internal waves
 642 in the oceanic thermocline at mid and low latitudes. *Dynamics of atmospheres and oceans*,
 643 **24** (1-4), 1–14.

644 Gregg, M. C., 1989b: Scaling turbulent dissipation in the thermocline. *J. Geophys. Res.*, **94**, 9686–
 645 9698.

646 Hebert, D. A., and S. M. de Bruyn Kops, 2006a: Predicting turbulence in flows with strong stable
 647 stratification. *Phys. Fluids*, **18** (6), 1–10.

648 Hebert, D. A., and S. M. de Bruyn Kops, 2006b: Relationship between vertical shear rate and
 649 kinetic energy dissipation rate in stably stratified flows. *Geophys. Res. Let.*, **33**, L06 602, doi:
 650 doi:10.1029/2005GL025071.

651 Henyey, F. S., J. Wright, and S. M. Flatté, 1986: Energy and action flow through the internal wave
 652 field: An eikonal approach. *Journal of Geophysical Research: Oceans*, **91** (C7), 8487–8495.

653 Johnson, H. L., and C. Garrett, 2004: Effects of noise on thorpe scales and run lengths. *Journal of*
654 *physical oceanography*, **34** (11), 2359–2372.

655 Klymak, J. M., and J. D. Nash, 2007: Estimates of mixing.

656 Kolmogorov, A. N., 1962: A refinement of previous hypotheses concerning the local structure
657 of turbulence in a viscous incompressible fluid at high Reynolds number. *J. Fluid Mech.*, **13**,
658 82–85.

659 Large, W. G., J. C. McWilliams, and S. C. Doney, 1994: Oceanic vertical mixing - a review and a
660 model with a nonlocal boundary-layer parameterization. *Rev. Geophys.*, **32**, 363–403.

661 Lindborg, E., 2006: The energy cascade in a strongly stratified fluid. *J. Fluid Mech.*, **550**, 207–242.

662 MacKinnon, J., and M. Gregg, 2003: Mixing on the late-summer new england shelvesoliboires,
663 shear, and stratification. *Journal of Physical Oceanography*, **33** (7), 1476–1492.

664 Maffioli, A., and P. A. Davidson, 2016: Dynamics of stratified turbulence decaying from a high
665 buoyancy Reynolds number. *J. Fluid Mech.*, **786**, 210–233.

666 Marra, J., R. Bidigare, and T. Dickey, 1990: Nutrients and mixing, chlorophyll and phytoplankton
667 growth. *Deep Sea Research Part A. Oceanographic Research Papers*, **37** (1), 127–143.

668 Marshall, J., and K. Speer, 2012: Closure of the meridional overturning circulation through south-
669 ern ocean upwelling. *Nature Geoscience*, **5** (3), 171.

670 Mashayek, A., C. P. Caulfield, and W. R. Peltier, 2013: Time-dependent, non-monotonic mixing
671 in stratified turbulent shear flows: implications for oceanographic estimates of buoyancy flux. *J.*
672 *Fluid Mech.*, **736**, 570–593.

673 Mashayek, A., C. P. Caulfield, and W. R. Peltier, 2017a: Role of overturns in optimal mixing in
674 stratified mixing layers. *J. Fluid Mech.*, **826**, 522–552.

675 Mashayek, A., H. Salehipour, D. Bouffard, C. P. Caulfield, R. Ferrari, M. Nikurashin, W. R.
676 Peltier, and W. D. Smyth, 2017b: Efficiency of turbulent mixing in the abyssal ocean circulation.
677 *Geophys. Res. Lett.*, **44**, 6296–6306.

678 Mater, B. D., S. K. Venayagamoorthy, L. St. Laurent, and J. N. Moum, 2015: Biases in thorpe-scale
679 estimates of turbulence dissipation. part i: Assessments from large-scale overturns in oceano-
680 graphic data. *Journal of Physical Oceanography*, **45** (10), 2497–2521.

681 Monismith, S. G., J. R. Koseff, and B. L. White, 2018: Mixing efficiency in the presence of
682 stratification: when is it constant? *Geophys. Res. Lett.*, **45**, 5627–5634.

683 Moum, J., M. Gregg, R. Lien, and M. Carr, 1995: Comparison of turbulence kinetic energy dis-
684 sipation rate estimates from two ocean microstructure profilers. *Journal of Atmospheric and*
685 *Oceanic Technology*, **12** (2), 346–366.

686 Moum, J. N., 1996: Energy-containing scales of turbulence in the ocean thermocline. *J. Geophys.*
687 *Res.-Oceans*, **101**, 14 095–14 109.

688 Osborn, T. R., 1980: Estimates of the local-rate of vertical diffusion from dissipation measure-
689 ments. *J. Phys. Oceanogr.*, **10**, 83–89.

690 Osborn, T. R., and C. S. Cox, 1972: Oceanic fine structure. *Geophysical & Astrophysical Fluid*
691 *Dynamics*, **3** (1), 321–345.

692 Overholt, M. R., and S. B. Pope, 1998: A deterministic forcing scheme for direct numerical sim-
693 ulations of turbulence. *Computers & Fluids*, **27**, 11–28.

694 Pacanowski, R., and S. Philander, 1981: Parameterization of vertical mixing in numerical models
695 of tropical oceans. *Journal of Physical Oceanography*, **11** (11), 1443–1451.

696 Palmer, M., G. Stephenson, M. Inall, C. Balfour, A. Düsterhus, and J. Green, 2015: Turbulence
697 and mixing by internal waves in the celtic sea determined from ocean glider microstructure
698 measurements. *Journal of Marine Systems*, **144**, 57–69.

699 Polzin, K. L., J. M. Toole, and R. W. Schmitt, 1995: Finescale parameterizations of turbulent
700 dissipation. *Journal of physical oceanography*, **25** (3), 306–328.

701 Pope, S. B., 2000: *Turbulent Flows*. Cambridge University Press, Cambridge.

702 Pope, S. B., 2001: *Turbulent flows*. IOP Publishing.

703 Portwood, G. D., S. M. de Bruyn Kops, J. R. Taylor, H. Salehipour, and C. P. Caulfield, 2016:
704 Robust identification of dynamically distinct regions in stratified turbulence. *J. Fluid Mech.*,
705 **807**, R2 (14 pages).

706 Rao, K. J., and S. M. de Bruyn Kops, 2011: A mathematical framework for forcing turbulence
707 applied to horizontally homogeneous stratified flow. *Phys. Fluids*, **23**, 065 110, doi:doi:10.1063/
708 1.3599704.

709 Riley, J. J., and S. M. de Bruyn Kops, 2003: Dynamics of turbulence strongly influenced by
710 buoyancy. *Phys. of Fluids*, **15** (7), 2047–2059.

711 Rorai, C., P. D. Mininni, and A. Pouquet, 2014: Turbulence comes in bursts in stably stratified
712 flows. *Physical Review E*, **89** (4), 043 002.

713 Salehipour, H., and W. Peltier, 2015: Diapycnal diffusivity, turbulent prandtl number and mixing
714 efficiency in boussinesq stratified turbulence. *Journal of Fluid Mechanics*, **775**, 464–500.

715 Salehipour, H., W. R. Peltier, C. B. Whalen, and J. A. MacKinnon, 2016: A new characterization
716 of the turbulent diapycnal diffusivities of mass and momentum in the ocean. *Geophys. Res. Lett.*,
717 **43** (7), 3370–3379.

718 Scotti, A., 2015: Biases in thorpe-scale estimates of turbulence dissipation. part ii: energetics
719 arguments and turbulence simulations. *Journal of Physical Oceanography*, **45** (10), 2522–2543.

720 Smyth, W. D., and J. N. Moum, 2000: Length scales of turbulence in stably stratified mixing
721 layers. *Phys. Fluids*, **12**, 1327–1342.

722 Sreenivasan, K. R., 1998: An update on the energy dissipation rate in isotropic turbulence. *Phys.*
723 *Fluids*, **10** (2), 528–529.

724 Sreenivasan, K. R., and R. A. Antonia, 1997: The phenomenology of small-scale turbulence.
725 *Annu. Rev. Fluid Mech.*, **29**, 435–472.

726 Thorpe, S., 2005: The turbulent ocean, 439 pp. *Cambridge University*.

727 Thorpe, S. A., 1977: Turbulence and mixing in a Scottish loch. *Philos. Trans. Roy. Soc. London*,
728 **A286**, 125–181.

729 Waite, M. L., 2011: Stratified turbulence at the buoyancy scale. *Phys. Fluids*, **23** (6), 066 602,
730 doi:10.1063/1.3599699.

731 Wang, L. P., S. Y. Chen, J. G. Brasseur, and J. C. Wyngaard, 1996: Examination of hypotheses in
732 the Kolmogorov refined turbulence theory through high-resolution simulations. Part 1. Velocity
733 field. *J. Fluid Mech.*, **309**, 113–156.

734 Warhaft, Z., 2000: Passive scalar in turbulent flows. *Annu. Rev. Fluid Mech.*, **32**, 203–240.

- 735 Waterhouse, A. F., and Coauthors, 2014: Global patterns of diapycnal mixing from measurements
736 of the turbulent dissipation rate. *Journal of Physical Oceanography*, **44** (7), 1854–1872.
- 737 Winters, K. B., and E. A. D’Asaro, 1996: Diascalar flux and the rate of fluid mixing. *Journal of*
738 *Fluid Mechanics*, **317**, 179–193.
- 739 Wunsch, C., and R. Ferrari, 2004: Vertical mixing, energy, and the general circulation of the
740 oceans. *Annu. Rev. Fluid Mech.*, **36**, 281–314.

741	LIST OF TABLES	
742	Table 1. Nondimensional simulation parameters and derived quantities.	38
743	Table 2. Dimensional simulation parameters and derived quantities. The values here	
744	have been made dimensional by setting the vertical domain height $L_z = 5\text{m}$ and	
745	kinematic viscosity $\nu = 10^{-6} \text{ m}^2\text{s}^{-1}$ in each simulation.	39

Label	$\tilde{L}_{x,y}$	\tilde{L}_z	$N_{x,y}$	N_z	Re	Fr	Pr	Fr_h	Fr_t	Re_h	Re_t	Re_B
A	2π	$\pi/4$	9216	1152	6452	0.0416	7	0.071	0.0019	7048	82755	12.1
B	2π	$\pi/4$	18432	2304	2410	0.0416	7	0.080	0.0025	23069	231575	57.5
C	2π	π	13104	6552	4679	0.1667	7	0.45	0.015	2985	25597	241.5

TABLE 1. Nondimensional simulation parameters and derived quantities.

Label	$L_{x,y}$	L_z	$\Delta_{x,y,z}$	N_0^2	$\langle \varepsilon \rangle_V$	L_O^V	L_K^V
A	40m	5m	4.3mm	$1.41 \times 10^{-5} \text{s}^{-2}$	$1.71 \times 10^{-10} \text{m}^2 \text{s}^{-3}$	5.6cm	8.7mm
B	40m	5m	2.2mm	$2.00 \times 10^{-4} \text{s}^{-2}$	$1.15 \times 10^{-8} \text{m}^2 \text{s}^{-3}$	6.3cm	3.0mm
C	10m	5m	0.76mm	$1.23 \times 10^{-4} \text{s}^{-2}$	$2.97 \times 10^{-8} \text{m}^2 \text{s}^{-3}$	14.8cm	2.4mm

TABLE 2. Dimensional simulation parameters and derived quantities. The values here have been made dimensional by setting the vertical domain height $L_z = 5\text{m}$ and kinematic viscosity $\nu = 10^{-6} \text{m}^2 \text{s}^{-1}$ in each simulation.

LIST OF FIGURES

- Fig. 1.** Normalized buoyancy, dissipation and vertical buoyancy flux on a vertical 2D slice extracted from Simulation C. Panels in the right column show a zoom of the boxed regions (note the changes in color bar). The white dashed lines indicate the location of the profile shown in Figure 2 42
- Fig. 2.** Vertical profiles of (a) buoyancy, (b) buoyancy flux, (c) displacement scale L_d , (d) turbulent kinetic energy dissipation rate, (e) turbulent potential energy dissipation rate, and (f) local mixing efficiency extracted from Simulation C. The profiles are taken from the location indicated with a white dashed line in Figure 1. The dashed red line in (a) is the sorted density profile. 43
- Fig. 3.** Dimensional lengthscales: horizontal domain size L_x , L_y , vertical domain size L_z , Thorpe scale L_T^V , Ozmidov scale L_O^V , Kolmogorov scale L_K^V , Batchelor scale L_B^V , and grid spacing $\Delta_{x,y,z}$. Simulation labels are given at the bottom of each series. The volume-averaged dissipation rate was used to calculate L_O^V , L_K^V , and L_B^V , and the Thorpe scale was calculated by sorting individual 1D density profiles and averaging the resulting Thorpe scale over all horizontal grid points. 44
- Fig. 4.** Vertical diffusivity estimated using the Osborn method κ_O^V (green circles), Osborn-Cox method κ_{O-C}^V (blue squares), and Thorpe method κ_T^V (magenta triangles), each calculated using data extracted from the full computational volume as defined in Eq. 23 and normalized by the turbulent vertical diffusivity diagnosed directly from the volume-averaged buoyancy flux, κ_d^V 45
- Fig. 5.** Autocorrelation function associated with the profile-averaged dissipation ε as a function of radial horizontal distance. 46
- Fig. 6.** PDFs of the normalized buoyancy flux B , kinetic energy dissipation rate ε , potential energy dissipation rate χ , and Thorpe scale L_T , each averaged over a single vertical profile and normalized by the volume average. For reference, the length of each vertical profile (5m) is indicated in terms of the Ozmidov length calculated using the volume averaged dissipation rate. 47
- Fig. 7.** Probability density function associated with the mixing efficiency, where χ and ε are calculated by averaging individual vertical profiles. Vertical dashed lines indicate the mean of each distribution. 48
- Fig. 8.** Estimates of the vertical diffusivity using the Osborn (green), Osborn-Cox (blue), Thorpe (magenta), and direct methods (red), calculated using n vertical profiles. Lines denote ± 1 standard deviation about the mean and the area between these limits is shaded. The dashed line indicates the vertical diffusivity calculated by directly averaging the flux over the full volume of the simulations as defined in Eq. 22. 49
- Fig. 9.** Standard deviation associated with quantities averaged over n vertical profiles, normalized by the 3D volume average. Dashed lines show the $n^{-1/2}$ scaling expected from the Central Limit Theorem. 50
- Fig. 10.** Fractional error associated with the Osborn relation (blue) and two assumptions used to derive the Osborn relation, specifically the assumption of constant flux coefficient (green) and a production-dissipation-buoyancy flux balance in the TKE budget (red). The values of

791

792

ε , B , P , and N^2 correspond to an average across the vertical domain and for the specified number of vertical profiles, e.g. $\langle \varepsilon \rangle_{z,n}$, and the averaging operators are omitted for clarity. . . . 51

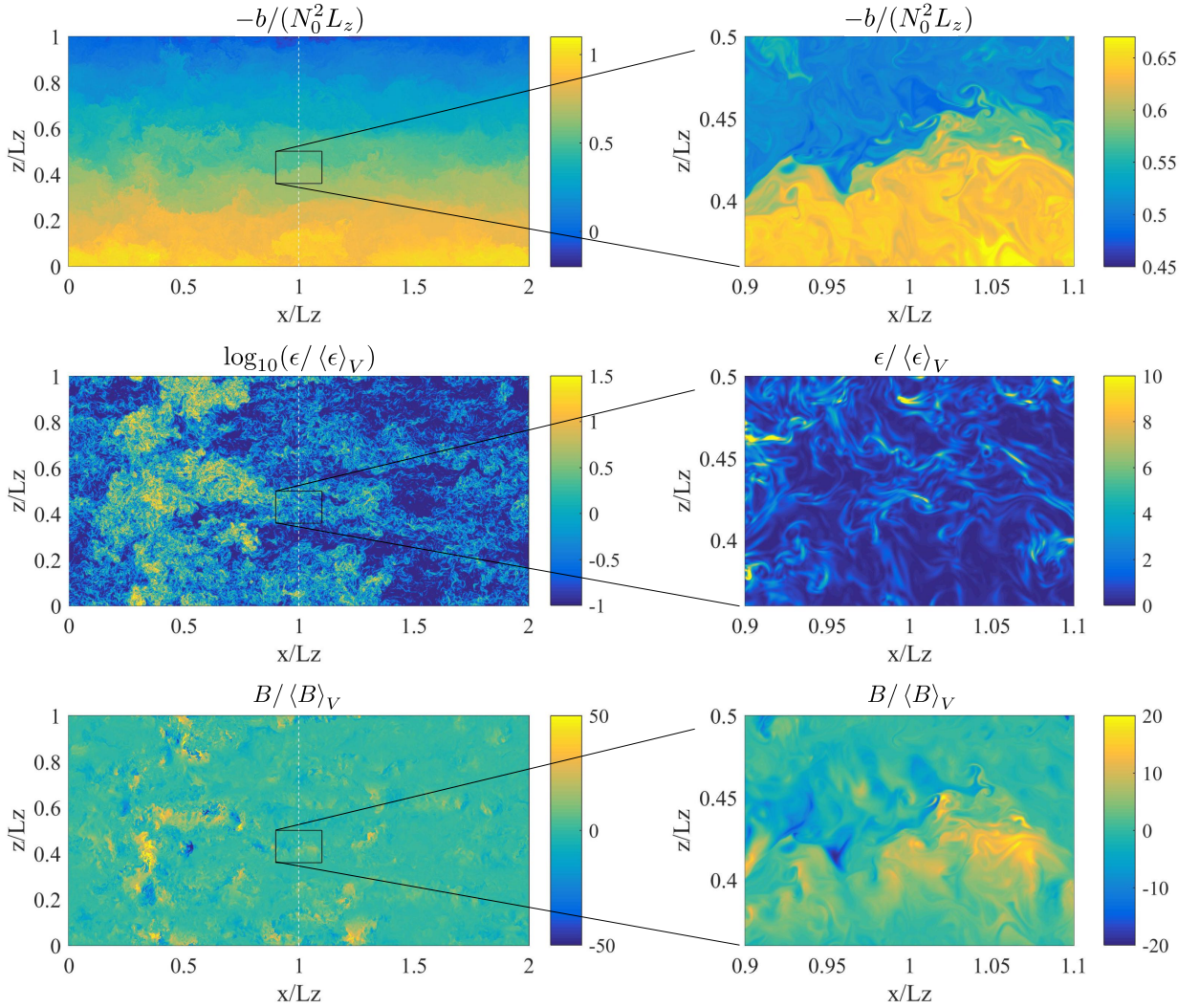
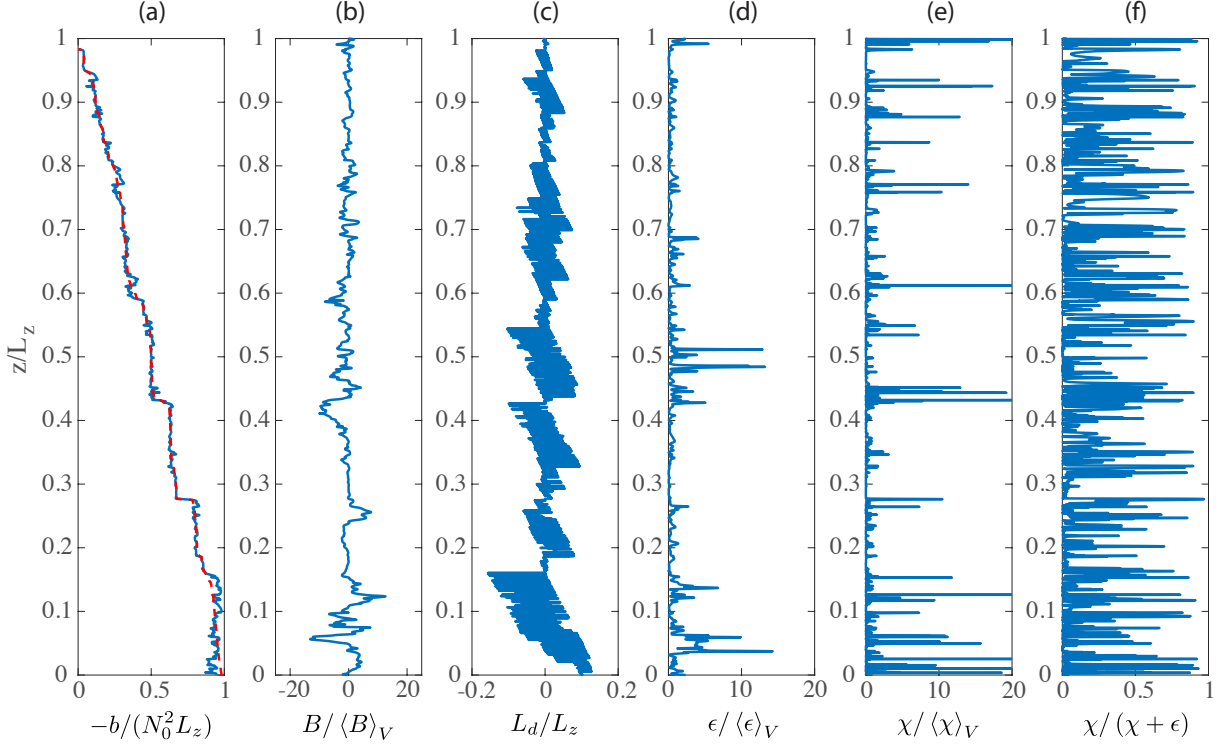
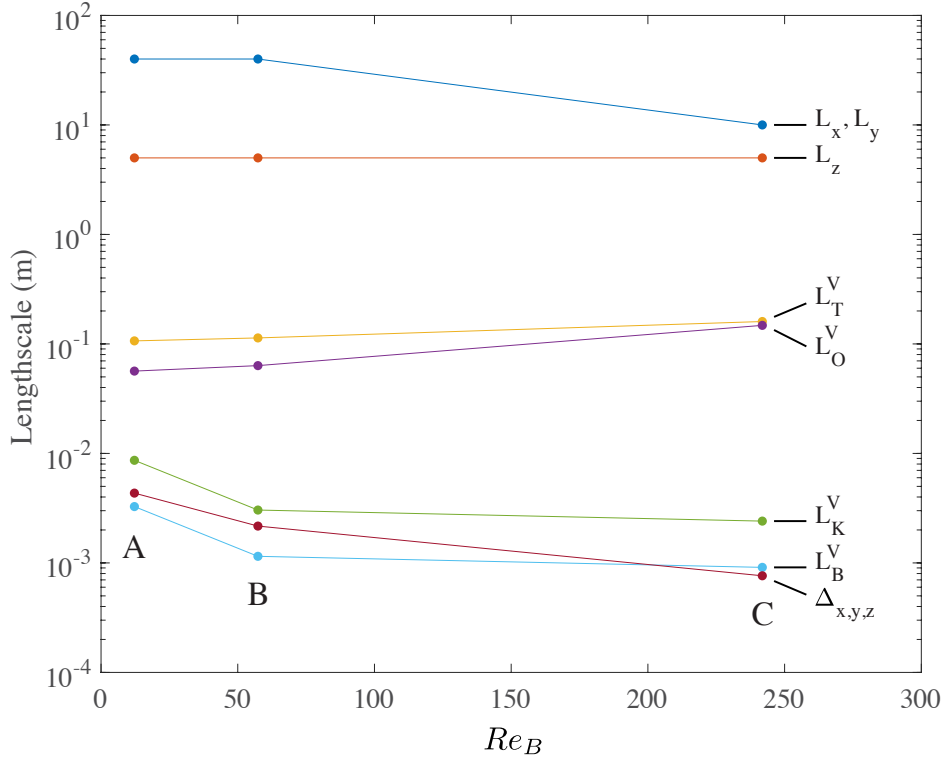


FIG. 1. Normalized buoyancy, dissipation and vertical buoyancy flux on a vertical 2D slice extracted from Simulation C. Panels in the right column show a zoom of the boxed regions (note the changes in color bar). The white dashed lines indicate the location of the profile shown in Figure 2



796 FIG. 2. Vertical profiles of (a) buoyancy, (b) buoyancy flux, (c) displacement scale L_d , (d) turbulent kinetic
 797 energy dissipation rate, (e) turbulent potential energy dissipation rate, and (f) local mixing efficiency extracted
 798 from Simulation C. The profiles are taken from the location indicated with a white dashed line in Figure 1. The
 799 dashed red line in (a) is the sorted density profile.



800 FIG. 3. Dimensional lengthscales: horizontal domain size L_x, L_y , vertical domain size L_z , Thorpe scale L_T^V ,
 801 Ozmidov scale L_O^V , Kolmogorov scale L_K^V , Batchelor scale L_B^V , and grid spacing $\Delta_{x,y,z}$. Simulation labels are
 802 given at the bottom of each series. The volume-averaged dissipation rate was used to calculate L_O^V, L_K^V , and L_B^V ,
 803 and the Thorpe scale was calculated by sorting individual 1D density profiles and averaging the resulting Thorpe
 804 scale over all horizontal grid points.

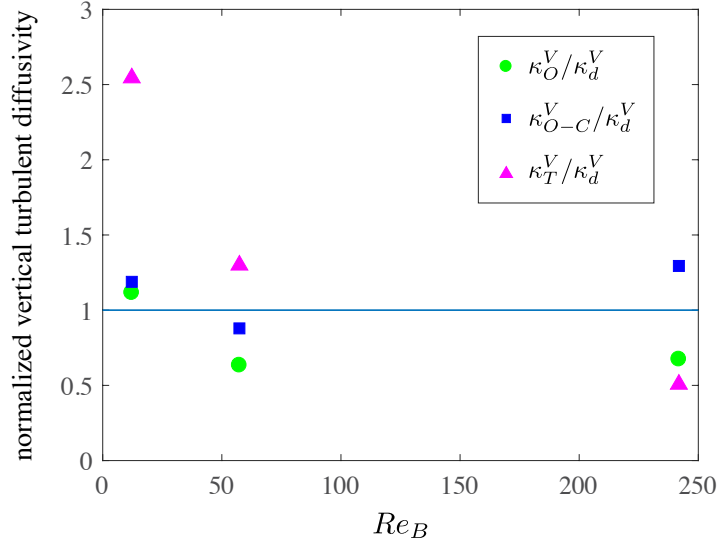
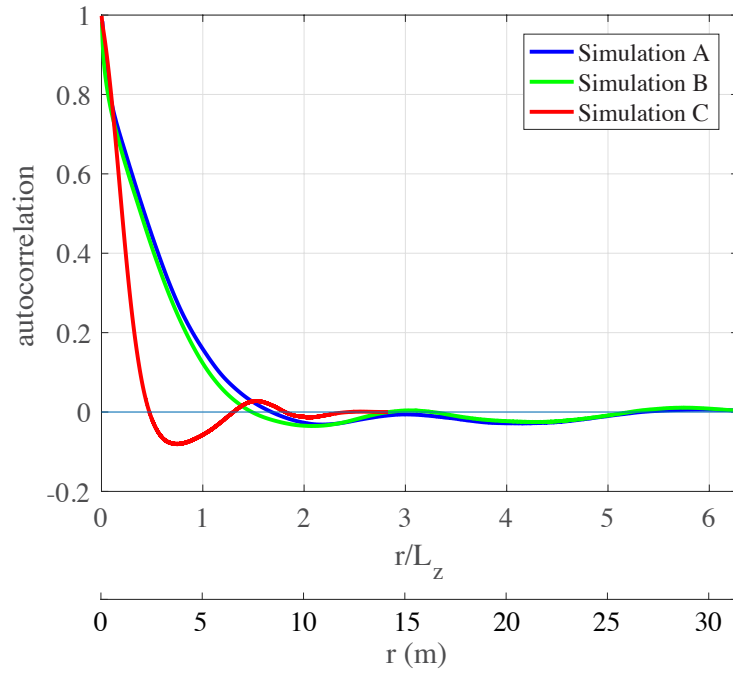


FIG. 4. Vertical diffusivity estimated using the Osborn method κ_O^V (green circles), Osborn-Cox method κ_{O-C}^V (blue squares), and Thorpe method κ_T^V (magenta triangles), each calculated using data extracted from the full computational volume as defined in Eq. 23 and normalized by the turbulent vertical diffusivity diagnosed directly from the volume-averaged buoyancy flux, κ_d^V .



809 FIG. 5. Autocorrelation function associated with the profile-averaged dissipation ε as a function of radial
810 horizontal distance.

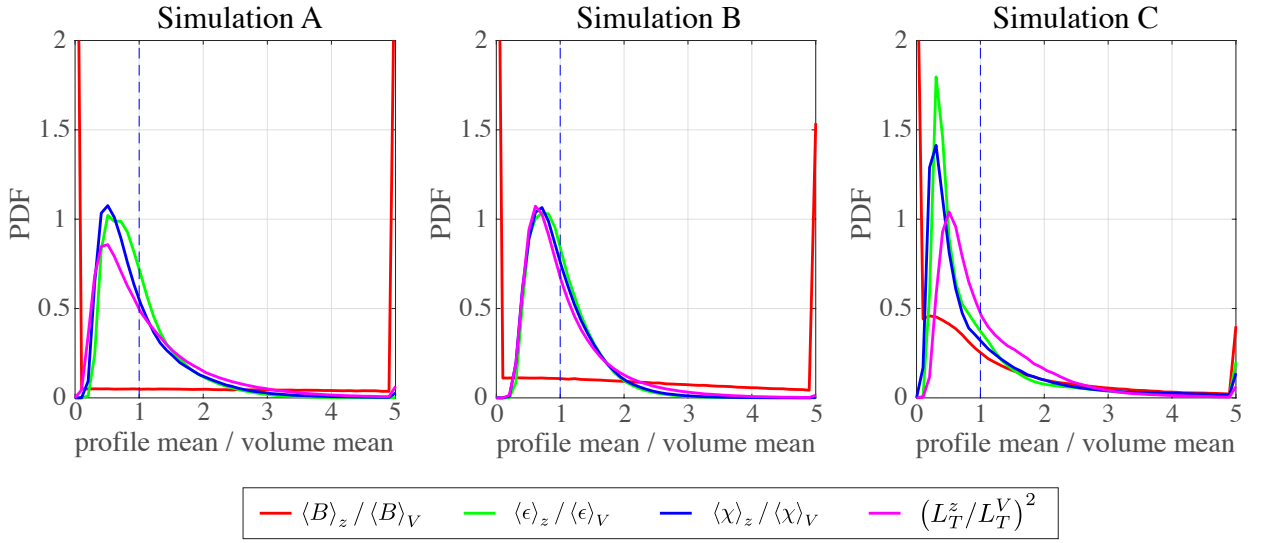
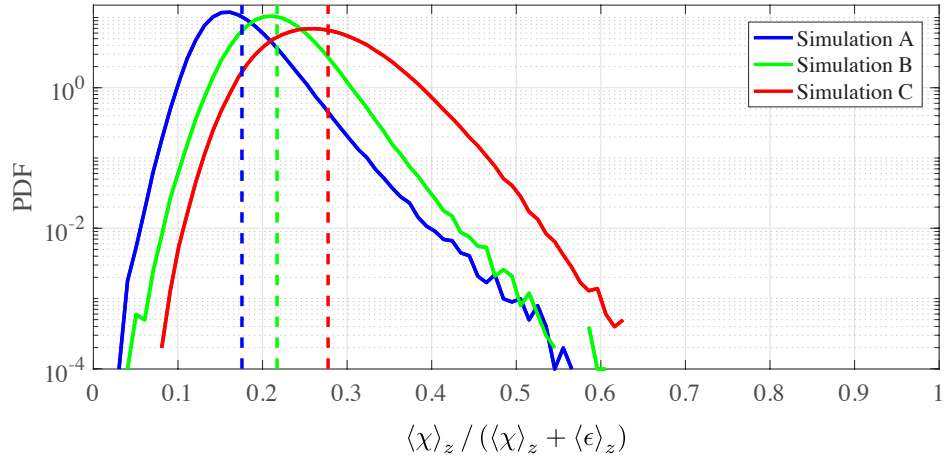


FIG. 6. PDFs of the normalized buoyancy flux B , kinetic energy dissipation rate ϵ , potential energy dissipation rate χ , and Thorpe scale L_T , each averaged over a single vertical profile and normalized by the volume average. For reference, the length of each vertical profile (5m) is indicated in terms of the Ozmidov length calculated using the volume averaged dissipation rate.



815 FIG. 7. Probability density function associated with the mixing efficiency, where χ and ϵ are calculated by
 816 averaging individual vertical profiles. Vertical dashed lines indicate the mean of each distribution.

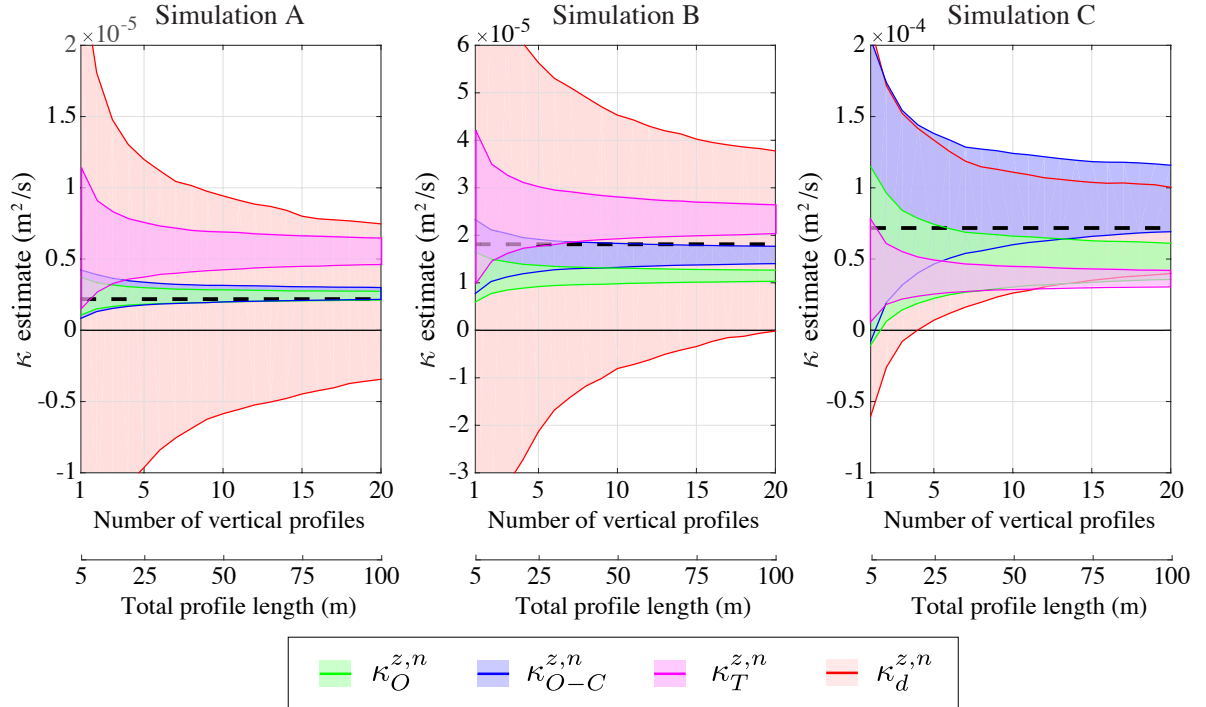


FIG. 8. Estimates of the vertical diffusivity using the Osborn (green), Osborn-Cox (blue), Thorpe (magenta), and direct methods (red), calculated using n vertical profiles. Lines denote ± 1 standard deviation about the mean and the area between these limits is shaded. The dashed line indicates the vertical diffusivity calculated by directly averaging the flux over the full volume of the simulations as defined in Eq. 22.

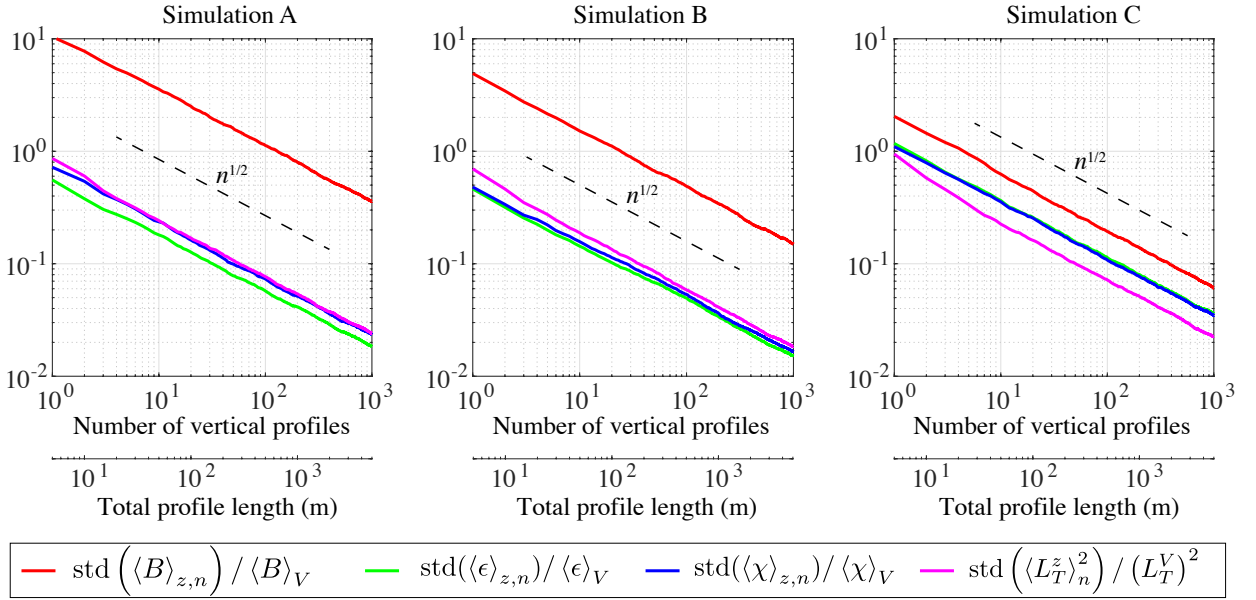


FIG. 9. Standard deviation associated with quantities averaged over n vertical profiles, normalized by the 3D volume average. Dashed lines show the $n^{-1/2}$ scaling expected from the Central Limit Theorem.

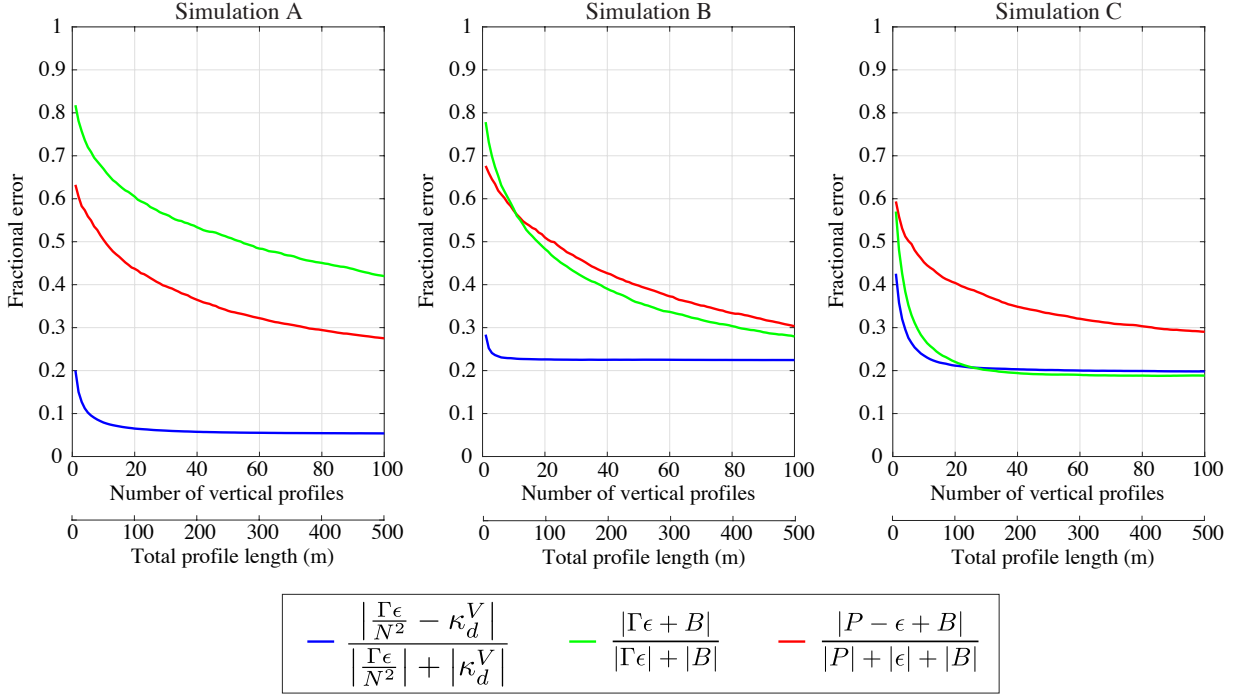


FIG. 10. Fractional error associated with the Osborn relation (blue) and two assumptions used to derive the Osborn relation, specifically the assumption of constant flux coefficient (green) and a production-dissipation-buoyancy flux balance in the TKE budget (red). The values of ϵ , B , P , and N^2 correspond to an average across the vertical domain and for the specified number of vertical profiles, e.g. $\langle \epsilon \rangle_{z,n}$, and the averaging operators are omitted for clarity.